

Microporous carbon from a biological waste-stiff silkworm for capacitive energy storage



Chengcheng Gong^a, Xinzhu Wang^a, Danhua Ma^b, Huifeng Chen^a, Shanshan Zhang^a, Zhixin Liao^{a,*}

^aSchool of Chemistry and Chemical Engineering, Southeast University, Nanjing 211189, PR China

^bSchool of Chemical Science and Technology, Yunnan University, Kunming 650091, PR China

ARTICLE INFO

Article history:

Received 16 May 2016

Received in revised form 14 October 2016

Accepted 17 October 2016

Available online 18 October 2016

Keywords:

carbon

biomass

stiff silkworm

Bombyx Batryticatus

supercapacitor

ABSTRACT

In general, carbon materials with high specific surface area (SSA), well-balanced pore size distributions, and appropriate content of heteroatom functionalities are essential to enhance the performance of electric double layer capacitors (EDLCs) for capacitive energy storage. In this study, a low-cost biological waste-stiff silkworm was first used as precursor for the synthesis of well-developed microporous carbon (SSMC) material by simple steps of carbonization and further activation. The SSMC was endowed with ultra-high SSA ($2523 \text{ m}^2 \text{ g}^{-1}$), large pore volume ($1.37 \text{ m}^3 \text{ g}^{-1}$), and high content of heteroatom functionalities ($\sim 3.5 \text{ at\% N}$ and $\sim 5.1 \text{ at\% O}$). EDLCs employed SSMC as active material showed high specific capacitance of 304 F g^{-1} and 256 F g^{-1} at current densities of 1 A g^{-1} and 20 A g^{-1} , respectively, suggesting the good rate capability. Symmetric-two-electrode test in aqueous electrolyte also delivered the specific capacitance of 235 F g^{-1} with the energy density of $\sim 7.9 \text{ Wh kg}^{-1}$. The findings confirmed the feasible way that using the eco-friendly biomass raw material to construct high performance capacitive energy storage device.

© 2016 Elsevier Ltd. All rights reserved.

1. Introduction

Supercapacitors, as a new type of energy storage device, have attracted tremendous attention because of their outstanding features, such as high power density, fast storage/release charge capability and outstanding cycle life. Supercapacitors can be categorized as electrical double layer capacitors (EDLCs), pseudo-capacitors or hybrid supercapacitors according to the charge storage mechanism [1]. Generally, ideal EDLCs provide capacitance through purely physical storage and release of electrostatic charges at the interface between inert carbonaceous-based electrode and electrolyte [2]. Pseudo-capacitors store charge Faradaically through transfer of charge between electrode (e.g. metal oxides/nitrides or conducting polymers) and electrolyte accomplished through electrosorption, redox reaction, and intercalation processes [2,3]. The hybrid capacitance arises from the combination of both processes [1]. The positive electrode obeys non-Faradaic mechanism and the other component comprising energy source material which utilizes reversible Faradaic reaction [3–5].

Compared with EDLCs, although pseudo-capacitors showed high specific capacitance in aqueous electrolytes, low electrical conductance, narrow potential window [1], poor compatibility with organic electrolytes, and the short cycle life have limited the practical application [6]. In addition, the lower abundance of pseudo-capacitive materials (e.g. nickel, cobalt or ruthenium) in the earth's crust means the high cost for commercial applications [1,7]. As the energy density is strongly dependent on the maximum voltage applied to the EDLCs, the choice of electrolyte may significantly affect the energy density [8]. Aqueous electrolytes typically withstand lower potential (0.6–1.4 V) in comparison with organic electrolytes (2.2–3.0 V) and ionic liquids (2.6–4.0 V) [8], meaning that electrodes in aqueous electrolytes deliver lower energy density [2–9]. Nevertheless, the advantages of using aqueous electrolytes include their very low cost, safety and high ionic conductivity [8].

Carbon based materials are preferred as EDLC electrodes owing to their high surface area (SSA), well-developed pore size distribution (PSD), relatively low cost, physical and chemical stability and its amphoteric nature that allows rich electrochemical properties from donor to acceptor state, and wide range of operating temperatures [2,8]. The appropriate heteroatom doping also plays a noticeable role, it not only can enhance the

* Corresponding author.

E-mail address: zxliao@seu.edu.cn (Z. Liao).

conductivity and wettability of carbon-based electrodes, but also extra capacitance that derived from the pseudo-capacitive effect of heteroatom functionalities will be gained [9]. Nano-porous carbon materials, such as activated carbon (AC) [9–12], carbon nanotubes [13], templated carbon [14,15], carbide-derived carbon [16] and graphene [6,17], etc., have been extensively studied employing as electrode materials for EDLCs [8]. Generally, a kind of electrode material only with a competitive ratio of performance to price, it could be able to bring the potential commercial value. Among these porous carbons, comparing with AC, other carbon materials inevitably suffer from the challenge [8,18]. As a matter of fact, AC has been commercially used as the EDLCs electrode material. Unfortunately, commercial AC-based supercapacitors usually had specific capacitance less than 200 F g^{-1} (in aqueous electrolyte) and low energy density values of $4 \sim 6 \text{ W h kg}^{-1}$ (in organic electrolyte) [6,8], which limits their more widespread applications in fields of electric and hybrid-electric vehicles, energy-efficient industrial equipment and smart-grid, etc.

By using nitrogen-containing biological raw materials as precursors without sophisticated chemical procedures for the formation of nitrogen-doped activated porous carbon has drawn extensive attention [9–12,18]. Among these raw materials, silkworm cocoon or natural silk based nitrogen-doped activated porous carbon have showed impressively electrochemical performance for various energy storage devices, such as supercapacitors, lithium-ion batteries, sodium-ion batteries, lithium-sulfur batteries and lithium-selenium batteries, etc. [9,19–22].

Stiff silkworm (*Bombyx batryticatus*) derives from silkworm (*Bombyx mori* L.) larva, which is infected by *Beauveria bassiana* before spinning silk and then resulting in stiffness and death [23]. Normally, as a forerunner of silk or silk protein, the silkworm cocoon is expensive, while the stiff silkworm is usually discarded as a uselessly biological waste. Therefore, using stiff silkworm as the precursor for the preparation of efficient AC undoubtedly will bring a low cost competitive advantage in comparison with using silk or silkworm cocoon as raw materials.

In this work, we first employed stiff silkworm as a low-cost precursor for the fabrication of high nitrogen-doping (~ 3.5 at%) porous carbon. The carbon had well-developed microporosity, large pore volume and ultrahigh SSA. Accordingly, EDLCs involved the obtained carbon showed enhanced specific capacitance of 304 F g^{-1} and 273 F g^{-1} at current density of 1 A g^{-1} in three-electrode test within the mass loading of activate material of $\sim 4 \text{ mg}$ and $\sim 7 \text{ mg}$, respectively. Single electrode in the two-symmetric electrode system delivered the specific capacitance of 253 F g^{-1} , and the entire device yielded a maximum energy density of $\sim 7.9 \text{ W h kg}^{-1}$. The electrochemical measurement results suggested that the synthesized porous carbon was a promising candidate electrode material for high performance capacitive energy storage device.

2. Experimental

The stiff silkworm was purchased from Simcere Kang Pharmaceutical, Nanjing. All reagents were used as-received without further purification. Distilled water was used throughout the experiment.

2.1. Material synthesis

The stiff silkworm was preliminary dried at 80°C for 2 hours and then carbonized at 500°C for 1 h under N_2 atmosphere with a heating rate of 5°C min^{-1} . The obtained residue was then thoroughly washed with 5% HCl solution and distilled water until neutral pH and then dried at 80°C to obtain non-activated carbon material, named as SSC. SSC was mixed with KOH (weight KOH/

weight $\text{Carbon} = 3$) and then activated at 750°C for 1 h under argon gas with a ramp rate of 5°C min^{-1} . The resulting product was washed with 5% HCl solution and distilled water until the neutral pH and then dried at 80°C to obtain the activated microporous carbon, named as SSMC.

2.2. Material characterizations

The powder X-ray diffraction data from 0.5° – 80° was measured on a Thermo ARL X'TRA instrument with Cu-K α radiation generated at 40 kV. The microscopic morphology and structure were observed by FEI Nova NanoSEM 450 scanning electron microscope working at 15 kV and JEOL JEM-200CX transmission electron microscope measurements operating at 200 kV. Raman spectra were carried out on Renishaw in Via 2000 Raman spectrometer with Ar laser wavelength of 458 nm. X-ray photoelectron spectroscopy analysis was taken on a Thermo Scientific Escalab 250Xi K-Alpha spectrometer with Al K α (1486.6 eV) as an X-ray source. The acquisition of high resolution spectrums were carried out on XPS PEAK41 software. Nitrogen sorption isotherm was measured on a Tristar II 3020 surface area analyzer (Micromeritics) at 77 K. Brunauer-Emmett-Teller model was performed to determine the specific surface area. The pore size distribution of micropore and mesopore was analyzed based on Horvath-Kawazoe and Barrett-Joyner-Halenda models, respectively.

2.3. Electrochemical measurements

A viscous slurry containing 85 wt% SSMC, 10 wt% acetylene black and 5 wt% polytetrafluoroethylene binder was uniformly mixed and then pressed onto the nickel foam ($10 \text{ mm} \times 10 \text{ mm}$) to fabricate the working electrode. The electrode was then dried at 100°C . In three-electrode test, a platinum electrode and a saturated calomel electrode (SCE) were used as counter and reference electrodes, respectively. Cyclic voltammetry curves were obtained at sweep rates from 5 mV s^{-1} to 150 mV s^{-1} . Galvanostatic charge-discharge profiles were obtained at current densities from 1 A g^{-1} to 30 A g^{-1} . Electrochemical impedance spectroscopy was measured with alternate current amplitude of 5 mV at the frequency from 10 mHz to 10 kHz. For two symmetrical-electrode system, the preparation of working electrodes followed the described procedures. All electrochemical studies were performed on a CHI660E electrochemical workstation (CH Instruments, US) using 6.0 M KOH aqueous as electrolyte. The specific capacitance (C , F g^{-1}) was calculated based on the galvanostatic charge-discharge records by using following equations:

$$C = \frac{I\Delta t}{m\Delta V} (\text{For 3 - electrode test})$$

$$C = \frac{4I\Delta t}{m\Delta V} (\text{For 2 - electrode test})$$

Where I is the constant discharge current (A), ΔV refers the potential window excluding the IR drop (V) within the discharge time Δt (s), and m is the total mass of active material in both electrodes (g).

The energy density (E , W h kg^{-1}) and power density (P , W kg^{-1}) of the two symmetrical-electrode test were calculated according to [14]:

$$E = \frac{1}{4} \times \frac{1}{2} C \Delta V^2 \frac{1}{3.6}$$

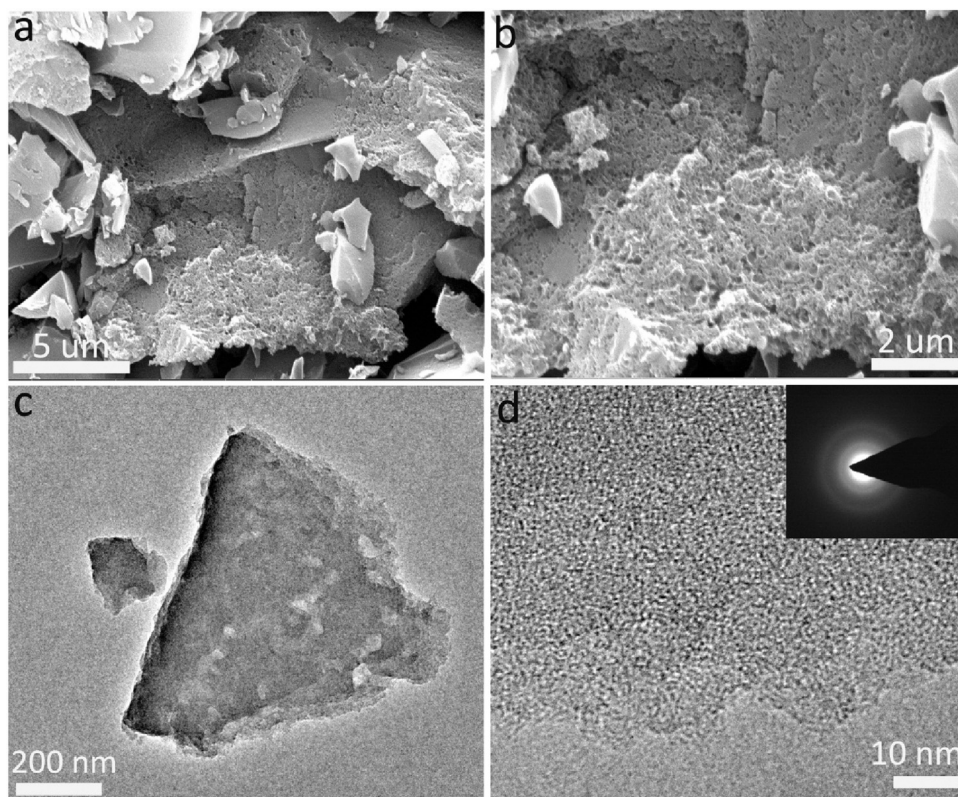


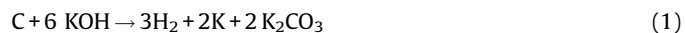
Fig. 1. The morphology characterization of SSMC sample. (a, b) SEM and (c) TME images at different magnifications; (d) HRTEM image and SAED pattern.

$$P = \frac{E \times 3600}{\Delta t}$$

Where C (F g^{-1}) represents the specific capacitance and ΔV (V) refers the potential range (not including IR drops) within the discharge time Δt (s). The divisor 4 is extrapolated to the total mass of active material and total mass of fully assembled cell based on an assumed value of 25 wt % for the active material in a packaged commercial cell.

3. Results and discussion

In this study, stiff silkworm-based activated carbon with well-developed microporosity and ultrahigh SSA was prepared *via* carbonization of dried precursor, followed by a typical activation using potassium hydroxide as the activator. As a result of the carbon matrix was etched into carbonate and releasing carbon oxide volatile gas with the increasing annealing temperature to 750 °C, the interconnected carbon walls were partly burnt out and massive pores were concurrently created [24]. The detailed activation mechanism might be described as the following equations [6,24]:



The surface morphology of porous carbon examined by scanning electron microscopy (SEM) and transmission electron microscopy (TEM). It could be seen from SEM images (Fig. 1a, b) that the SSMC sample exhibited loose block aggregates with highly interconnected 3D honeycomb-like micro-structure. Macropores with several hundred nanometers and large mesopores with dozens of nanometers were revealed incorporated into the porous carbon matrix. Generally, these relatively large scale porous structures were favorable for the rapid ions diffusion and charges transfer for EDLCs electrode material [24]. The TEM image shown in Fig. 1c suggested the distinctly porous characteristics, which accorded well with the observed records form SEM. In addition, the high resolution TEM (HRTEM) image (Fig. 1d) and selected area electron diffraction (SAED) pattern (Fig. 1d inset) demonstrated the amorphous nature of the carbon material.

X-ray photoelectron spectroscopy (XPS) was carried out to analyze the nitrogen doping and understand chemical states of each element. There were three peaks concentrated upon 284.6 eV, 405.7 eV and 533.2 eV corresponding to C 1s, N 1s and O 1s, respectively (Fig. 2a). Fittings the spectra to each element suggested that SSMC mainly contained carbon (~91.4 at%) along with small amount of nitrogen (~3.5 at%) and oxygen (~5.1 at%). As shown in Fig. 2b, the HR C 1s spectrum might be resolved into four individual peaks centered on 284.6 eV (C—C), 285.2 eV (C—N), 286.5 eV (C—O), and 288.4 eV–290.3 eV (C=O/C=C), respectively [24]. The N 1s signals presented in Fig. 2c implied the existence of three types of nitrogen-based groups including the hexagonal pyridinic N (N-6), pyrrolic nitrogen (N-5) and oxidized N (N-X), which characteristic binding energy were located at 398.4 eV, 400.3 eV and 402.4 eV, respectively [25]. Three types oxygen-functionalities corresponding to adsorbed oxygen (~531.2 eV), O—C=O (~533.1 eV) and C=O (534.0 eV–536.0 eV) could be extracted from the HR O 1s spectrum (Fig. 2d) [25]. It was well known that appropriate heteroatoms doping could bring about

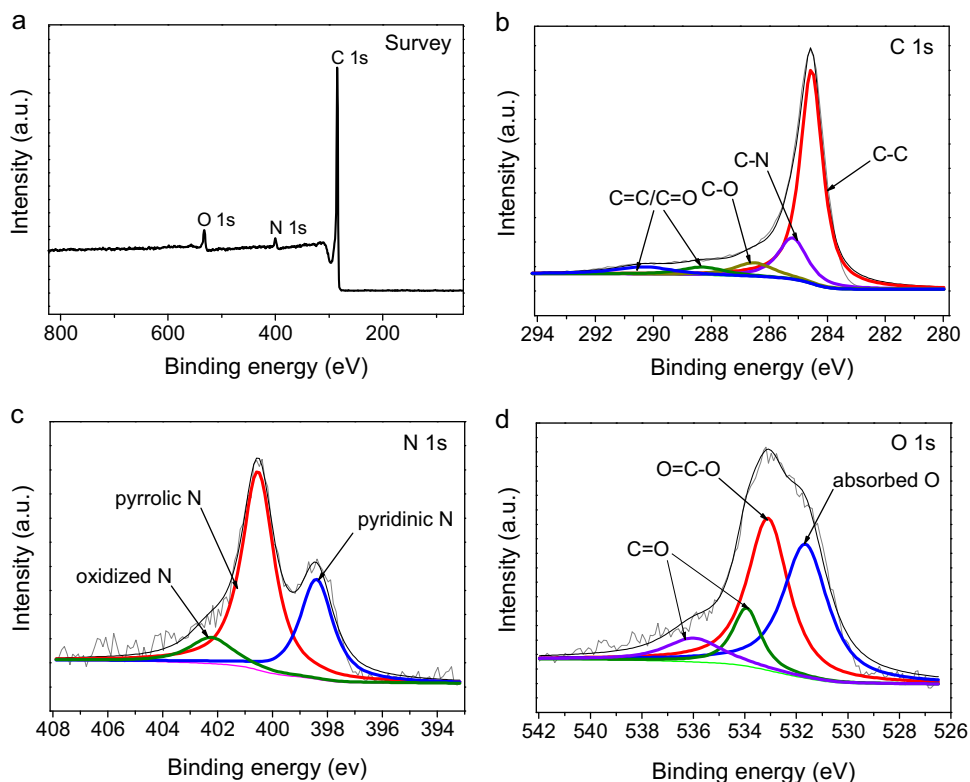


Fig. 2. Chemical elements analysis of SSMC material. (a) XPS spectra; and (b, c, d) high-resolution XPS spectrum analysis of C 1s, N 1s and O1s, respectively.

considerable improvement of specific capacitance because the heteroatoms induce pseudo-capacitive behaviour and improve the polar properties of carbon materials [9].

Raman spectroscopy and X-ray diffraction (XRD) techniques were employed to further confirm the micro-structure features analyzed by TEM. Raman spectra exhibits in Fig. 3a showed two

characteristic peaks of D-band and G-band at $\sim 1345\text{ cm}^{-1}$ and $\sim 1590\text{ cm}^{-1}$, respectively. The D-band was representative of the disorder- or defect-induced features [12,26]. The G-band was corresponded to the 2D hexagonal lattice in-plane stretching vibration of sp^2 -bonded carbon atoms (E_{2g} phonon), which was beneficial for enhancing the electrical conductivity [27]. The G-

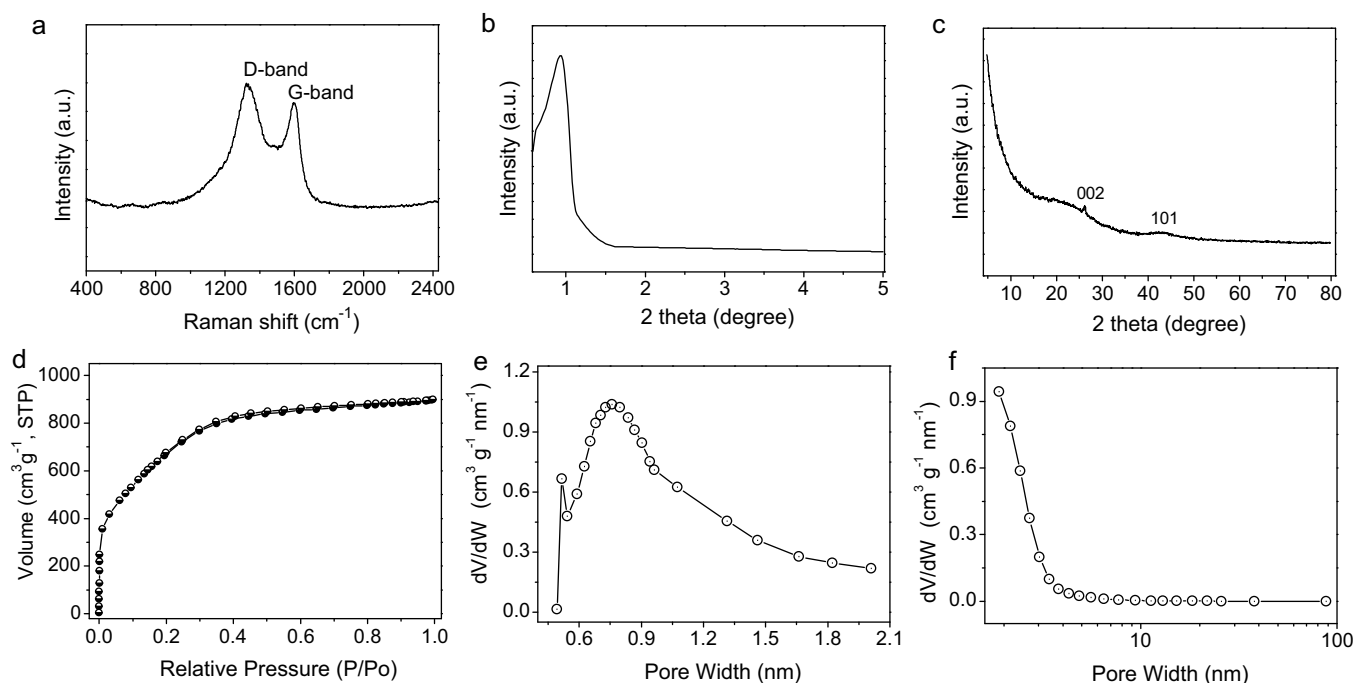


Fig. 3. Structural characterization of SSMC sample. (a) Raman spectra; (b) SAXS pattern; (c) XRD pattern; (d) nitrogen sorption isotherm; and (e, f) size analyses of micropores and mesopores based on Horvath-Kawazoe and Barrett-Joyner-Halenda models, respectively.

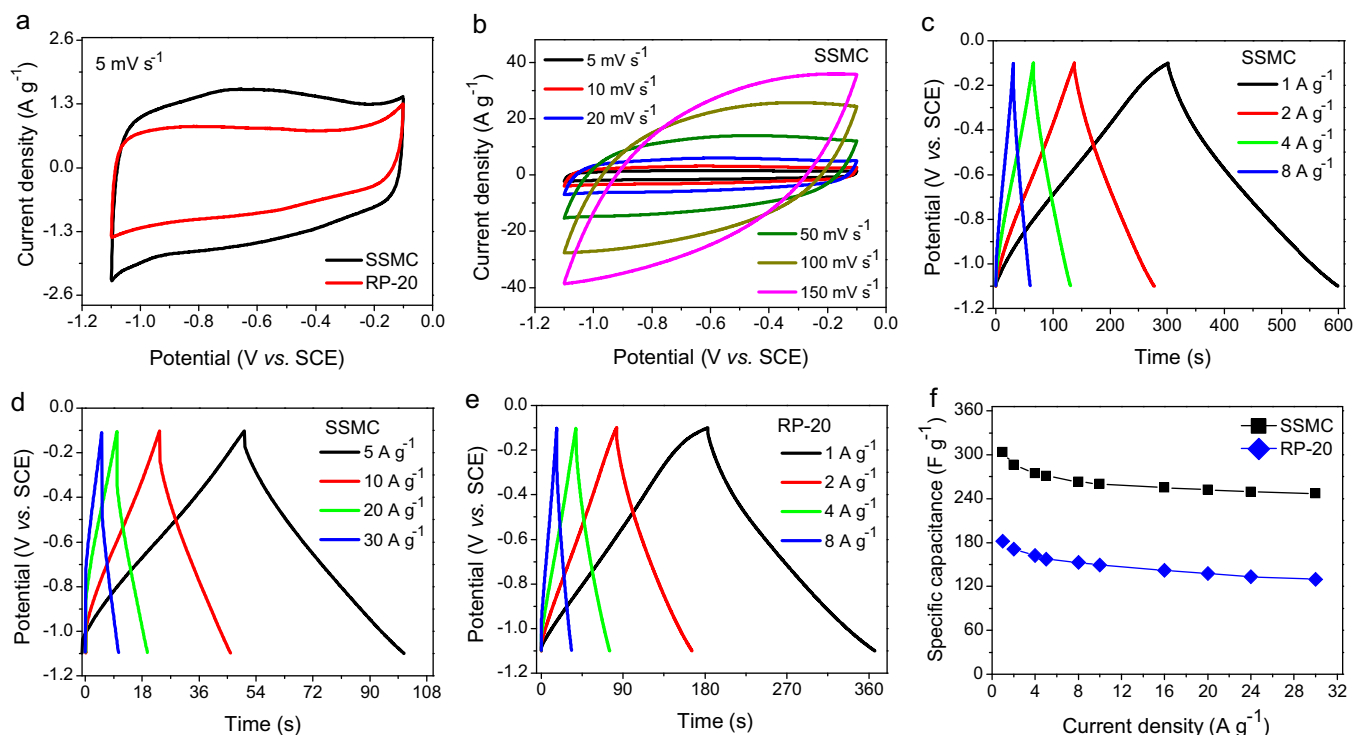


Fig. 4. Electrochemical performance of SSMC and RP-20 based electrode examined by three-electrode test. (a, b) cyclic voltammetry curves at the sweep rate from 5 mV s^{-1} to 150 mV s^{-1} ; (c–e) galvanostatic charge-discharge records at current loadings from 1 A g^{-1} to 30 A g^{-1} ; (f) the specific capacitance as a function of the current density. (The mass loading was about 4 mg and geometrical area of working electrode was $\sim 1 \text{ cm}^2$).

band was correlated to the (002) diffraction peak in XRD pattern as well [27]. The relative intensity ratio I_G/I_D was always used to evaluate the structural crystallinity degree of carbon materials. The I_G/I_D value of SSMC was calculated as ~ 0.84 , indicating the very low graphitized carbon structure [24]. In wide-angle XRD pattern (Fig. 3c), two diffraction peaks around $2\theta = 26.3^\circ$ and 43.4° are attributed to the (002) and (101) planes of graphite, respectively, which matched the diffraction planes of the hexagonal graphitic carbon. However, the fact that weak (002) diffraction peak intensity suggested the low degree of crystallization [20]. Analysis results based on Raman spectra and XRD pattern were in agreement with the amorphous structure observed by HRTEM. Noteworthy, the intense diffraction in the low-angle scattering in XRD pattern (2θ below 10°) implied the high density of microporosity [6,9]. The small-angle X-ray scattering (SAXS) pattern (Fig. 3b) of SSMC sample exhibited the well-resolved diffraction peak with $2\theta = 0.92^\circ$, indicating the existence of mesopores [28].

In general, SSA and pore size distributions were two key factors for high performance EDLCs. Thus, the nitrogen adsorption-desorption isotherm was performed to further examine the porous characteristics of obtained material, and the detailed results were listed in Fig. 3d–f. According to the IUPAC classification, the SSMC sample clearly showed a typical type-I sorption isotherm but with a very slight type-H4 hysteresis loop (Fig. 3d). It meant that the existence of very abundant of micropores and small amounts of mesopores [9,19], which was consistent with the XRD and SAXS analyses. Based on the Brunauer-Emmett-Teller calculation model analysis at $P/P_0 = 0.30$, the BET SSA of the material is up to $\sim 2523 \text{ m}^2 \text{ g}^{-1}$. The total pore volume was calculated as $\sim 1.37 \text{ cm}^3 \text{ g}^{-1}$ determined at $P/P_0 = 0.95$ and the microporous volume ($\sim 1.09 \text{ cm}^3 \text{ g}^{-1}$) accounted for 79.6% of the total volume. The micropore and mesopore size analyses based on Horvath-Kawazoe and Barrett-Joyner-Halenda models were exhibited in Fig. 3e and f,

respectively. They showed that the pore size distributions of micropores mainly focused on $\sim 0.8 \text{ nm}$ ($0.6 \sim 1 \text{ nm}$), and the mesopores mainly with the average pore width of $2 \sim 3 \text{ nm}$.

On the basis of the above characterizations and analyses, it could be demonstrated that the stiff silkworm-based porous carbon not only possessed high content of nitrogen functionalities but was endowed with amazing SSA, well-developed microporosity as well as low proportion of meso-porosity and macroporosity. Normally, mesopores and macropores were supposed to supply convenient and smooth ion-transfer accesses as well as buffer pools for rapid ions attachment [24]. Micropores generally offered sufficient space for ions/charges storage and release [24]. In addition, the *in-situ* nitrogen doping could enhance the electrical conductivity, wettability and induced pseudo-capacitive behaviour [9], which further improved the utilization ratio of electro-active sites that based on SSA [24].

To evaluate the electrochemical capacitance performance of the SSMC material, cyclic voltammetry (CV), galvanostatic charge-discharge (GCD), electrochemical impedance spectroscopy measurements and cycle stability measurements were conducted in 6 M KOH aqueous electrolyte. The capacitive performance of RP-20 [29,30], one of the most used activated carbon in commercial supercapacitor industry for practical application, was also tested under the identical condition. The three-electrode test results within the potential window ranging from -0.1 to -1.1 V (vs. SCE) were given in Fig. 4. The mass loading of the two activate materials was about 4 mg and geometrical area of working electrode is $\sim 1 \text{ cm}^2$. Fig. 4a showed quasi-rectangular CV curves lacking redox hump at low scan rate of 5 mV s^{-1} , suggesting the nearly-ideal electric double layer behavior during the charge-discharge process. Obviously, the dramatically enhanced current response suggested more capacitive energy could be stored in SSMC electrode than RP-20 [30]. With the scan rate increased, the rectangle gradually distorted but still symmetrical (Fig. 4b). It was as the result of the

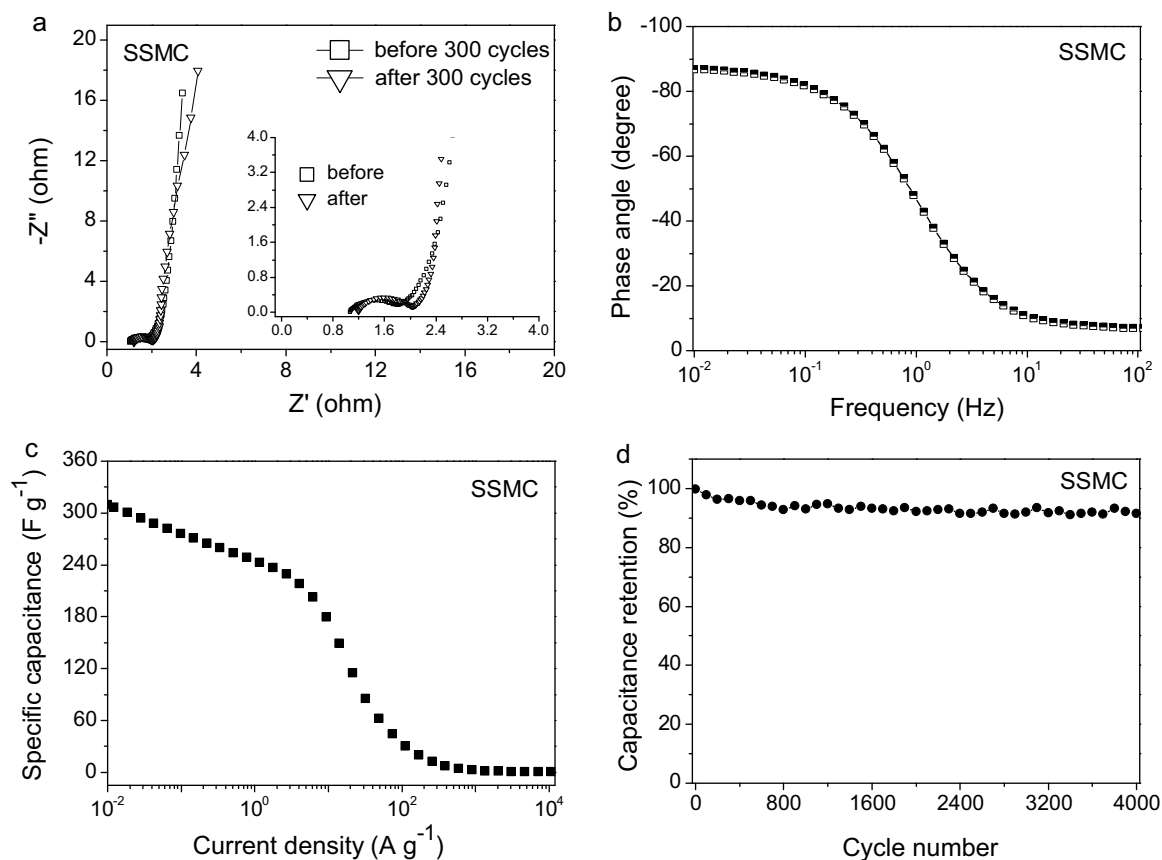


Fig. 5. (a) Nyquist plot before and after 300 cycles; (b) Bode plot derived from the alternating current impedance spectroscopy; (c) the specific capacitance as a function of the frequency; and (d) cycle stability measurement at the current density of 5 A g^{-1} for 4000 cycles. The mass loading of SSMC on working electrode (1 cm^2) was $\sim 4 \text{ mg}$.

electrode polarization effect and then the effect gradually becomes the controlling step. Detailed explanation might be described that the electrolyte ions diffusion mass transfer rate was relatively slow that could not meet the demand of the electrode needed when at large current densities or high scan rates.

The isosceles triangle GCD curves of SSMC and RP-20 electrodes with different IR drops at various current densities were profiled in Fig. 4c–e. These isosceles triangle records signified the highly reversible in the course of charging and discharging. The IR drop at the start of discharge process was usually used to estimate the equivalent internal resistance (ESR) [6], and then determined the effective maximum voltage range during that discharge process. The specific capacitance of SSMC and RP-20 electrodes has been calculated on the basis of the GCD data at various current densities, as shown in Fig. 4f. SSMC-based EDLCs delivered high specific capacitance values of 304 F g^{-1} and 275 F g^{-1} at the current density of 1 A g^{-1} and 5 A g^{-1} , respectively. Even at the current density 30 A g^{-1} , the specific capacitance of the fabricated device was still as high as 248 F g^{-1} (81.6% of 304 F g^{-1}), suggesting a good rate capability. The comparison of capacitive performance among previous reports about biomass-based ACs electrode material as listed in Table 1 [10,26,30–36]. Comparatively, the RP-20 electrode under the identical condition only displayed a capacitance of 181 F g^{-1} and 130 F g^{-1} at current loadings of 1 A g^{-1} and 30 A g^{-1} , respectively. Combined with the CV and GCD curves, it suggested that SSMC electrode had higher capacitive storage capacities and superior rate capability in comparison with the commercial RP-20.

The Nyquist plot and Bode plot of SSMC electrode resulted from the electrochemical impedance spectroscopy measurement in a frequency ranging from 0.01 Hz to 10 kHz were displayed in Fig. 5a and b, respectively. The Nyquist plot exhibited representative

impedance characteristics of EDLCs, namely, a virtually-vertical line reflected the nearly capacitive response at the low frequency [6]. The semicircle section at the high frequency region meant the bulk electrolyte resistance and the charge transfer resistance [15]. The short nearly 45° slope of Warburg segment at the intermediate frequency range revealed the fast diffusion/transfer of ions [20,30], leading to a small IR drop at the initiation of the discharge process (0.014 V at the current density of 1 A/g), suggesting a very low voltage impedance (or ERS, $\sim 3.5 \text{ Ohm}$) in the test cell [6]. Before 300 cycles, the electrolyte resistance (R_e , $\sim 1.06 \text{ Ohm}$) and charge transfer resistance (R_{ct} , $\sim 0.72 \text{ Ohm}$) have been quantitated by the left intersection with the horizontal real axis (Z') and the right intercept of the semi-circle segment, respectively. After 300 cycles,

Table 1

Comparison of the electrochemical performance of bio-derived activated porous carbon.

Precursor	SSA ^a	SC ^b	Testing conditions ^c	Ref.
Cashmere	1358	236	6 M KOH (3 mg, 1 A g^{-1})	[10]
Broad beans shell	655	202	6 M KOH (5 mg, 0.5 A g^{-1})	[26]
Shiitake mushroom	2988	306	6 M KOH (2.4 mg, 1 A g^{-1})	[30]
Water bamboo	2352	268	6 M KOH (1.2 mg, 1 A g^{-1})	[31]
Albumen	1227	255	1 M H_2SO_4 (7 mg, 1 A g^{-1})	[32]
Oil palm kernel shell	727	210	1 M KOH (4 mg, 0.5 A g^{-1})	[33]
Stem bark	1212	320	6 M KOH (3 mg, 0.5 A g^{-1})	[34]
Willow catkins	1776	292	6 M KOH (3 mg, 1 A g^{-1})	[35]
Pomelo mesocarps	975	245	2 M KOH (0.08 mg, 0.5 A g^{-1})	[36]
Stiff silkworm	2523	304	6 M KOH (4 mg, 1 A g^{-1})	This work
		273	6 M KOH (7 mg, 1 A g^{-1})	

^a BET specific surface area ($\text{m}^2 \text{ g}^{-1}$).

^b specific capacitance (F g^{-1}).

^c mass loading of active materials within electrodes at current densities in the aqueous electrolyte.

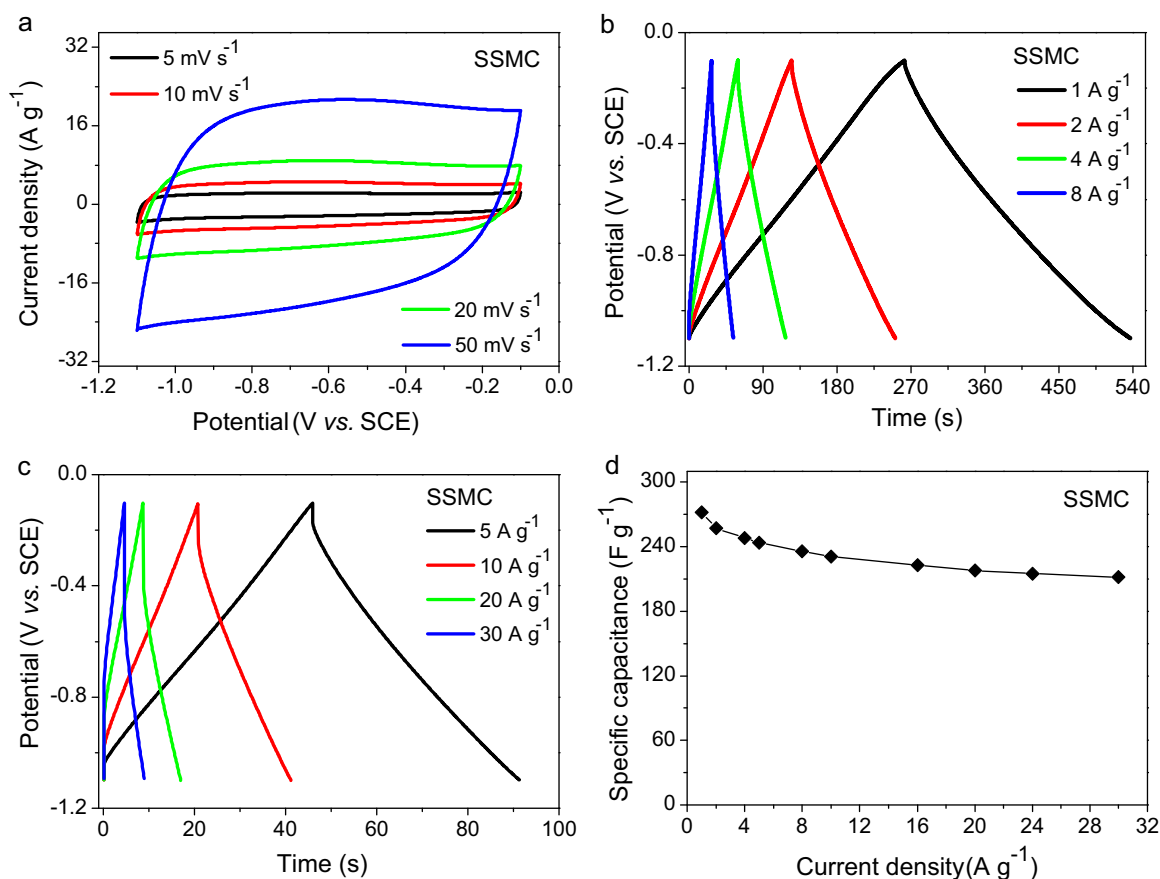


Fig. 6. Electrochemical performance of SSMC-based electrode examined by three-electrode test. (a, b) Cyclic voltammetry curves at the sweep rate from 5 mV s^{-1} to 150 mV s^{-1} ; (b, c) galvanostatic charge-discharge records at current loadings from 1 A g^{-1} to 30 A g^{-1} ; (d) the specific capacitance as a function of the current density. (The mass loading was about 7 mg and geometrical area of working electrode was $\sim 1 \text{ cm}^2$).

the R_e and R_{ct} were $\sim 1.19 \text{ Ohm}$ and $\sim 0.84 \text{ Ohm}$, respectively, illustrating the impedance showed slight change (Fig. 5a). This result signified that almost no deterioration of the electrode materials occurred during the repetitive charge-discharge cycling [15]. The nearly -90° phase angle in the Bode plot confirmed the ideally capacitive behavior at the low-frequency region of $\sim 0.01 \text{ Hz}$ (Fig. 5b). The characteristic frequency (f_0) anchored around -45° phase angle was about 1.04 Hz , corresponding the time constant τ_0 ($=1/f_0$) of $\sim 0.96 \text{ s}$. Generally, the much shorter time constant meant the faster ion/charge transfer [6,14,27]. Based on the Nyquist plot, the specific capacitance values were also calculated from the equation [15]:

$$C = \frac{-1}{2 \times \pi \times f \times m \times Z''}$$

where m is the loading mass of active material (g), f is the frequency (Hz) and Z'' is the imaginary part of the impedance (Ohm). The capacitance values were quantified as 309, 274, 246, 169 and 34 F g^{-1} at frequencies of about 0.01, 0.1, 1, 10 and 100 Hz , respectively (Fig. 5c). The values decreased with the frequencies increase might be due to the inner pores could not available be accessible to electrolyte ions at higher frequencies [15]. Cycle stability measurement under the current density of 5 A g^{-1} was exhibited in Fig. 5d. The 94.5% specific capacitance retention over 4000 cycles implied the excellent cycling stability.

It was well known that the mass of the active material also influenced the measured results, especially mass measurement errors could be significant when handling and weighing microgram

sized electrodes [37]. The increased mass loading also benefited the volumetric capacitance, which is important for practical applications [38]. When the mass loading increased to $\sim 7 \text{ mg}$ within the same geometrical area of working electrode (1 cm^2), the specific capacitances were 273 F g^{-1} at current density of 1 A g^{-1} (Fig. 6b, d), which approximated to 90% of the measured results that 304 F g^{-1} at 1 A g^{-1} with the activate material of $\sim 4 \text{ mg}$, indicating that SSMC matrix had effective access to the electrolyte without geometric or electric hindrance or diffusion limitation [38].

Symmetric two-electrode system that closer to actual device was also performed to evaluate the electrochemical performance. Both the approximate rectangle CV curves showed Fig. 7a and the quasi-isosceles triangle GCD records exhibited in Fig. 7b reflected the purely electric double layer capacitive features. Based on the GCD records, single electrode exhibited high specific capacitance of 235 F g^{-1} and 183 F g^{-1} at current densities of 1 A g^{-1} and 8 A g^{-1} in 6.0 M KOH , respectively (Fig. 7c). Fig. 7d showed the Ragone plot that rendered the relationship of the energy density and power density. The two-electrode cell based on SSMC material delivered a maximum energy density of $\sim 7.9 \text{ Wh kg}^{-1}$ with the power density of $\sim 234 \text{ W kg}^{-1}$ at the current loading of 1 A g^{-1} . The obtained energy density of the SSMC-based device was not only higher than the traditional commercial activated carbon-based electrode material (typically the energy density with the order of $4\text{--}6 \text{ Wh kg}^{-1}$ in organic electrolyte), but also higher than the previously reported bio-carbon based symmetric EDLCs devices under similar calculation equations (detailed scatters inserted in Fig. 7d) [10,12,27,30,39].

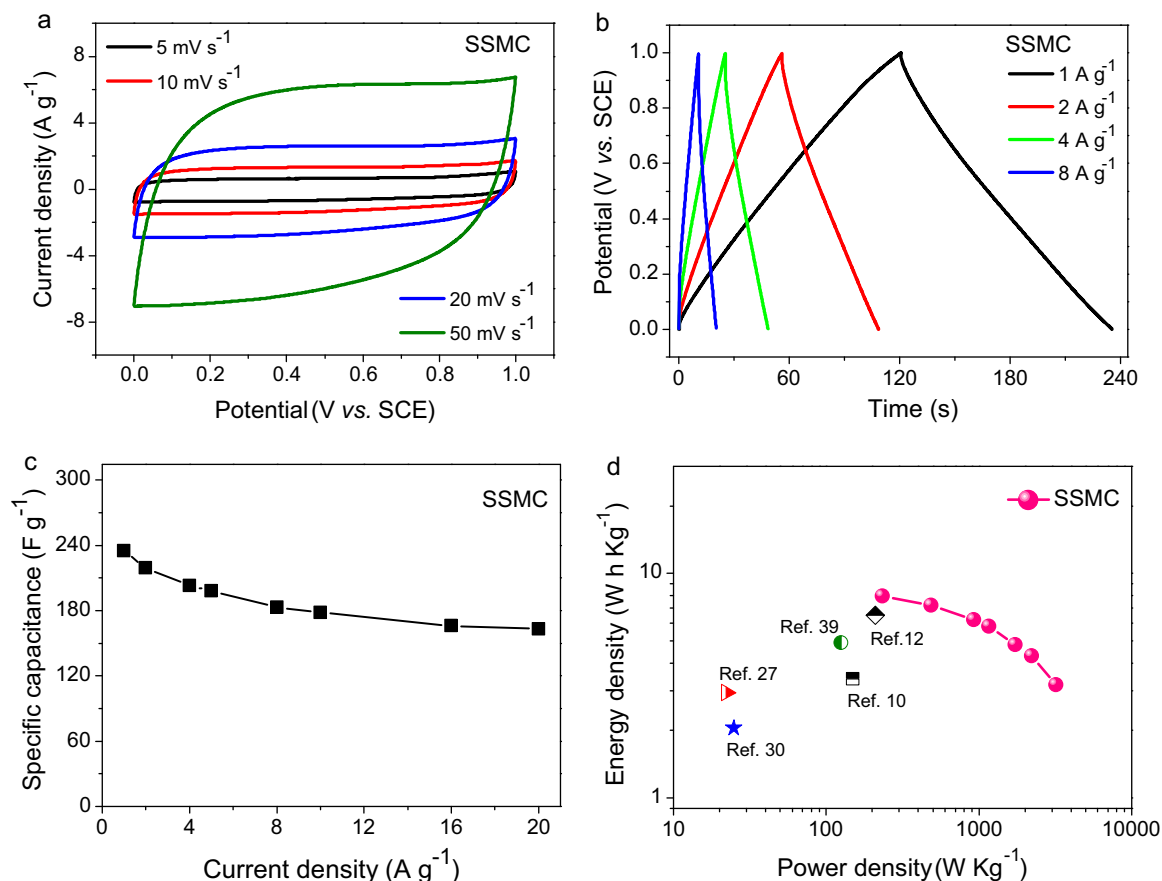


Fig. 7. Electrochemical performance evaluation of SSMC material was carried out on two-electrode symmetrical test. (a) CV curves at sweep rates of 5–50 mV s⁻¹; (b) GCD records at the current density from 1 A g⁻¹ to 8 A g⁻¹; (c) dependence of the specific capacitance on different current densities, (d) Ragone plot. (Activated material loaded on each electrode was ~3 mg).

5. Conclusions

As a summary, stiff silkworm was first employed as a novel precursor for the synthesis of carbon electrode material for capacitive energy storage device. The obtained carbon was endowed with an ultra-high SSA, well-developed microporosity together with rich nitrogen doping. The nitrogen-doped microstructure not only provided enough activated attachment sites for ions to anchor, but brought the non-ignorable pseudo-capacitance effects. Therefore, single carbon electrode exhibited high specific capacitance of 304 F g⁻¹ and 235 F g⁻¹ at current density of 1 A g⁻¹ in three- and two-electrode tests, respectively. The entire symmetric device delivered a high energy density of ~7.9 W h kg⁻¹ with the power density of ~234 W kg⁻¹. In view of stiff silkworm as a low-cost and eco-friendly biomass waste, simple and convenient formation process, and outstanding capacitance storage capability, SSMC is highly expected as activate material for high-performance commercial supercapacitors.

References

- [1] S.G. Krishnan, M.V. Reddy, M. Harilal, B. Vidyadharan, I.I. Misnon, M.H. AbRahim, J. Ismail, R. Jose, Characterization of MgCo₂O₄ as an electrode for high performance supercapacitors, *Electrochim. Acta* 161 (2015) 312.
- [2] V. Aravindan, M.V. Reddy, S. Madhavi, S.G. Mhaisalkar, G.V.S. Rao, B.V.R. Chowdari, Hybrid supercapacitor with nano-TiP₂O₇ as intercalation electrode, *J. Power Sources* 196 (2011) 8850.
- [3] B. Das, M. Behm, G. Lindbergh, M.V. Reddy, B.V.R. Chowdari, High performance metal nitrides MN (M = Cr, Co) nanoparticles for non-aqueous hybrid supercapacitors, *Adv. Powder Technol.* 26 (2015) 783.
- [4] V. Aravindan, M.V. Reddy, S. Madhavi, G.V.S. Rao, B.V.R. Chowdari, Electrochemical Performance of α -MnO₂ Nanorods/Activated Carbon Hybrid Supercapacitor, *Nanosci. Nanotechnol. Lett.* 4 (2012) 724.
- [5] V. Aravindan, W. Chuiling, M.V. Reddy, G.V.S. Rao, B.V.R. Chowdari, S. Madhavi, Carbon coated nano-LiTi₂(PO₄)₃ electrodes for non-aqueous hybrid supercapacitors, *Phys. Chem. Chem. Phys.* 14 (2012) 5808.
- [6] Y. Zhu, S. Murali, M.D. Stoller, K.J. Ganesh, W. Cai, P.J. Ferreira, A. Pirkle, R.M. Wallace, K.A. Cychoz, M. Thommes, D. Su, E.A. Stach, R.S. Ruoff, Carbon-Based Supercapacitors Produced by Activation of Graphene, *Science* 332 (2011) 1537.
- [7] Y. Wu, R. Balakrishna, M.V. Reddy, A.S. Naira, B.V.R. Chowdari, S. Ramakrishna, Functional properties of electrospun NiO/RuO₂ composite carbon nanofibers, *J. Alloys Compd.* 517 (2012) 69.
- [8] W. Gu, G. Yushin, Review of nanostructured carbon materials for electrochemical capacitor applications: advantages and limitations of activated carbon, carbide-derived carbon, zeolite-templated carbon, carbon aerogels, carbon nanotubes, onion-like carbon, and graphene, *Wiley Interdiscip. Rev. Energy Environ.* 3 (2014) 424.
- [9] Y.S. Yun, S.Y. Cho, J. Shim, B.H. Kim, S.J. Chang, S.J. Baek, Y.S. Huh, Y. Tak, Y.W. Park, S. Park, H.J. Jin, Microporous Carbon Nanoplates from Regenerated Silk Proteins for Supercapacitors, *Adv. Mater.* 25 (2013) 1993.
- [10] L. Zhou, H. Cao, S. Zhu, L. Hou, C. Yuan, Hierarchical micro-/mesoporous N- and O-enriched carbon derived from disposable cashmere: a competitive cost-effective material for high-performance electrochemical capacitors, *Green Chem.* 17 (2015) 2373.
- [11] F. Gao, J. Qua, Z. Zhao, Z. Wang, J. Qiu, Nitrogen-doped activated carbon derived from prawn shells for high-performance supercapacitors, *Electrochim. Acta* 190 (2016) 1134.
- [12] J. Deng, T. Xiong, F. Xu, M. Li, C. Han, Y. Gong, H. Wang, Y. Wang, Inspired by bread leavening: one-pot synthesis of hierarchically porous carbon for supercapacitors, *Green Chem.* 17 (2015) 4053.
- [13] A.R. John, P. Arumugam, Open ended nitrogen-doped carbon nanotubes for the electrochemical storage of energy in a supercapacitor electrode, *J. Power Sources* 277 (2015) 387.
- [14] J. Zhao, H. Lai, Z. Lyu, Y. Jiang, K. Xie, X. Wang, Q. Wu, L. Yang, Z. Jin, Y. Ma, J. Liu, Z. Hu, Hydrophilic Hierarchical Nitrogen-Doped Carbon Nanocages for Ultrahigh Supercapacitive Performance, *Adv. Mater.* 27 (2015) 3541.

- [15] Z. Wang, Y. Xiong, S. Guan, A simple CaCO_3 -assisted template carbonization method for producing nitrogen doped porous carbons as electrode materials for supercapacitors, *Electrochim. Acta* 188 (2016) 757.
- [16] B. Dyatkin, O. Gogotsi, B. Malinovsky, Y. Zozulya, P. Simon, Y. Gogotsi, High capacitance of coarse-grained carbide derived carbon electrodes, *J. Power Sources* 306 (2016) 32.
- [17] J. Wang, B. Ding, Y. Xu, L. Shen, H. Dou, X. Zhang, Crumpled Nitrogen-Doped Graphene for Supercapacitors with High Gravimetric and Volumetric Performances, *ACS Appl. Mater. Interfaces* 7 (2015) 22284.
- [18] M. Sevilla, R. Mokaya, Energy storage applications of activated carbons: supercapacitors and hydrogen storage, *Energy Environ. Sci.* 7 (2014) 1250.
- [19] J. Zhang, Y. Cai, Q. Zhong, D. Lai, J. Yao, Porous nitrogen-doped carbon derived from silk fibroin protein encapsulating sulfur as a superior cathode material for high-performance lithium-sulfur batteries, *Nanoscale* 7 (2015) 17791.
- [20] J. Hou, C. Cao, F. Idrees, X. Ma, Hierarchical Porous Nitrogen-Doped Carbon Nanosheets Derived from Silk for Ultrahigh-Capacity Battery Anodes and Supercapacitors, *ACS Nano* 9 (2015) 2556.
- [21] M. Jia, C. Mao, Y. Niu, J. Hou, S. Liu, S. Bao, J. Jiang, M. Xu, Z. Lu, A selenium-confined porous carbon cathode from silk cocoons for Li-Se battery applications, *RSC Adv.* 5 (2015) 96146.
- [22] Y.S. Yun, K.Y. Park, B. Lee, S.Y. Cho, Y.U. Park, S.J. Hong, B.H. Kim, H. Gwon, H. Kim, S. Lee, Y.W. Park, Hyoung-Joon Jin, Kisuk Kang, Sodium-Ion Storage in Pyroprotein-Based Carbon nanoplates, *Adv. Mater.* 27 (2015) 6914.
- [23] X. Jiang, Z. Zhang, Y. Chen, Z. Cui, L. Shi, Structural elucidation and in vitro antitumor activity of a novel oligosaccharide from *Bombyx batryticatus*, *Carbohydr. Polym.* 103 (2014) 434.
- [24] L. Qie, W. Chen, H. Xu, X. Xiong, Y. Jiang, F. Zou, X. Hu, Y. Xin, Z. Zhang, Y. Huang, Synthesis of functionalized 3D hierarchical porous carbon for high-performance supercapacitors, *Energy Environ. Sci.* 6 (2013) 2497.
- [25] H. Zhu, J. Yin, X. Wang, H. Wang, X. Yang, Microorganism-Derived Heteroatom-Doped Carbon Materials for Oxygen Reduction and Supercapacitors, *Adv. Funct. Mater.* 23 (2013) 1305.
- [26] G. Xu, J. Han, B. Ding, P. Nie, J. Pan, H. Dou, H. Li, X. Zhang, Biomass-derived porous carbon materials with sulfur and nitrogen dual-doping for energy storage, *Green Chem.* 17 (2015) 1668.
- [27] J. Wang, L. Shen, Y. Xu, H. Dou, X. Zhang, Lamellar-structured biomass-derived phosphorus and nitrogen-co-doped porous carbon for high-performance supercapacitors, *New J. Chem.* 39 (2015) 9497.
- [28] Z. Chen, J. Wen, C. Yan, L. Rice, H. Sohn, M. Shen, M. Cai, B. Dunn, Y. Lu, High-Performance Supercapacitors Based on Hierarchically Porous Graphite Particles, *Adv. Energy Mater.* 1 (2011) 551.
- [29] L. Zhang, F. Zhang, X. Yang, K. Leng, Y. Huang, Y. Chen, High-performance supercapacitor electrode materials prepared from various pollens, *Small* 9 (2013) 1342.
- [30] P. Cheng, S. Gao, P. Zang, X. Yang, Y. Bai, H. Xu, Z. Liu, Z. Lei, Hierarchically porous carbon by activation of shiitake mushroom for capacitive energy storage, *Carbon* 93 (2015) 315.
- [31] J. Li, Q. Wu, Water bamboo-derived porous carbons as electrode materials for supercapacitors, *New J. Chem.* 39 (2015) 3859.
- [32] C. Yuan, L. Zhou, S. Zhu, H. Cao, L. Hou, Albumen-Derived Hierarchical Porous N- and O-Enriched Carbon towards High-Performance Electrochemical Capacitors, *J. Electrochem. Soc.* 162 (2015) A781.
- [33] I.I. Misnon, N.K.M. Zain, R. Abd Aziz, B. Vidyadharan, R. Jose, Electrochemical properties of carbon from oil palm kernel shell for high performance supercapacitors, *Electrochim. Acta* 174 (2015) 78.
- [34] T. Wei, X. Wei, Y. Gao, H. Li, Large scale production of biomass-derived nitrogen-doped porous carbon materials for supercapacitors, *Electrochim. Acta* 169 (2015) 186.
- [35] L. Xie, G. Sun, F. Su, X. Guo, Q. Kong, X. Li, X. Huang, L. Wan, W. Song, K. Li, C. Lv, C. Chen, *J. Mater. Chem. A* 4 (2016) 1637.
- [36] H. Peng, G. Ma, K. Sun, Z. Zhang, Q. Yang, Z. Lei, Nitrogen-doped interconnected carbon nanosheets from pomelo mesocarps for high performance supercapacitors, *Electrochim. Acta* 190 (2016) 862.
- [37] M.D. Stoller, R.S. Ruoff, Best practice methods for determining an electrode material's performance for ultracapacitors, *Energy Environ. Sci.* 3 (2010) 1294.
- [38] T. Lin, I.-W. Chen, F. Liu, C. Yang, H. Bi, F. Xu, F. Huang, Nitrogen-doped mesoporous carbon of extraordinary capacitance for electrochemical energy storage, *Science* 350 (2015) 1508.
- [39] P. Hao, Z. Zhao, J. Tian, H. Li, Y. Sang, G. Yu, H. Cai, H. Liu, C.P. Wong, A. Umar, Hierarchical porous carbon aerogel derived from bagasse for high performance supercapacitor electrode, *Nanoscale* 6 (2014) 12120.